npj | flexible electronics

Article

Published in partnership with Nanjing Tech University

https://doi.org/10.1038/s41528-025-00497-2

Logic-device-inspired mechanical computing system based on three-dimensional active components

Check for updates

Jun Hyun Park[1,9], Jang Hwan Kim[3,4,9], Ha Uk Chung[5,9], Jun Seok Choe[1], Hyokyeong Kim[6], Su Eon Lee[1], Simon Kim[1], Ho Jun Jin[1], Jiwoong Kim[6] ✉, Heon Lee[7] ✉, Jaehwan Kim[8] ✉ & Bong Hoon Kim[1,2] ✉

Mechanical computing, utilizing mechanical deformation to perform calculations, has attracted significant attention as an innovative computing strategy for achieving high accuracy and exceptional physical robustness. However, its reliance on passive mechanical displacement limits its applicability for complex computations. This study presents a novel system that enables active light signal modulation through reversible mechanical deformation by integrating soft and 3D electronics. The proposed system features: 1) Optical fibers with optimized 3D cracks embedded in a low-modulus, high-elongation material, enabling strain-induced multimodal transitions. 2) Maximized stress concentration on the cracked fibers under strain, allowing them to function as active components for light modulation, which facilitates complex logic calculations and validates truth tables. 3) Multifunctional vibration sensing capabilities, illustrating the scalability of strain inputs and the potential for dynamic applications, such as soft robotics. These findings underscore the potential of this approach as a computational platform for mechanical motion-based technologies.

Mechanical computing is a data processing and calculation strategy that relies on the physical displacement and interaction of mechanical devices[1]. Owing to the operation mechanism based on mechanical motion, mechanical computing systems can maintain reliable performance even under harsh environmental conditions, such as extreme temperatures[2], radiation exposure[3], and signal interference[4,5]. In addition, the precise and sophisticated design of these systems ensures consistently high calculation accuracy, enabling computations with minimal errors and enhancing robustness against external changes[6–9]. These advantages have made mechanical computing an attractive technology for applications requiring precise mechanical deformations, such as advanced manufacturing systems and space engineering.

Despite these advantages, several intrinsic challenges remain in expanding the accessibility and applicability of mechanical computing. Conventional mechanical computing systems primarily employ high-modulus, low-elongation materials throughout the entire system, except for specific deformable elements, such as joints[10,11]. This design provides high strength and stiffness but makes the system susceptible to repetitive deformation and material fatigue. Moreover, the inherent limitations of systems composed of high-modulus materials[12–15] pose significant challenges for dynamic applications, such as wearable devices and soft robotics involving repetitive movements and complex motions with multi-dimensional nonlinear deformation. In this context, adopting low-modulus, high-elongation materials in mechanical computing systems presents a promising solution[16–19], offering flexibility and stretchability. Integrating low-modulus materials throughout the system ensures reliability even under repetitive displacement and prolonged loading while achieving greater spatial freedom of operation under multidimensional nonlinear deformations[20,21]. In addition, system configurations with low-modulus materials enable high sensitivity to environmental changes, supporting sophisticated and rapid data processing essential for dynamic applications.

Electronic computing systems are typically designed by combining passive and active components based on the required functions[22–24]. Passive components[25,26], such as resistors and capacitors, are suitable for transmitting or regulating signals but cannot modulate or amplify signal flow. By contrast, active components[27–29], such as diodes and transistors, perform the

[1]Department of Robotics and Mechatronics Engineering, DGIST, Daegu, Republic of Korea. [2]Center for Physical AI, DGIST, Daegu, Republic of Korea. [3]Department of Materials Science and Engineering, Ajou University, Suwon, Republic of Korea. [4]Department of Energy Systems Research, Ajou University, Suwon, Republic of Korea. [5]School of Biomedical Engineering, Korea University, Seoul, Republic of Korea. [6]Department of Materials Science and Engineering, Soongsil University, Seoul, Republic of Korea. [7]Department of Materials Science and Engineering, Korea University, Seoul, Republic of Korea. [8]School of Mechanical System Engineering, Kumoh National Institute of Technology (KIT), Gumi, Republic of Korea. [9]These authors contributed equally: Jun Hyun Park, Jang Hwan Kim, Ha Uk Chung. ✉e-mail: jwk@ssu.ac.kr; heonlee@korea.ac.kr; kimjh8729@kumoh.ac.kr; bonghoonkim@dgist.ac.kr

functions of passive components and enable advanced signal processing and complex logic calculations by modulating and amplifying signal flow[30–34]. In comparison, mechanical computing systems typically rely on passive computation derived from the deterministic behavior of mechanical components[35,36]. Thus, they are optimized for specific tasks but face challenges in implementing the active signal modulation capabilities provided by active components of electronic computers. This limitation leads to challenges with data processing, dynamic adjustments, and executing complex operations. Therefore, integrating active components into mechanical computing systems is necessary to meet the demands of increasingly complex modern computing tasks and provide adaptable, dynamic operations in diverse environments.

This study introduces a mechanical computing system integrating soft and three-dimensional (3D) electronics. The system employs mechanically guided 3D optical fibers as active components to modulate light transmission for highly complex computations while functioning as a vibration sensor. The key features of the proposed mechanical computing system are as follows: i) The first mechanical computing system incorporating soft electronics. The intrinsically flexible optical fiber-based mechanical computing system is built on a stretchable silicone elastomeric substrate, which induces mechanical deformation of optical fiber through substrate elongation. Incorporating low-modulus and high-elongation materials throughout the entire system enables nonlinear deformation in multidimensional space. ii) An active signal modulation capability similar to that of a diode in electronic computing systems is first demonstrated through the mechanically guided 3D deformation of optical fibers with cracks. The 3D structural transitions of the cracked optical fiber facilitate multimodal conversion between the on/off states of light transmission, enabling active light modulation. The morphology of the cracks is precisely designed to efficiently alter the light transmission path through stress concentration, as supported by simulation studies. In addition, multiple 3D multimodal optical fiber diodes are integrated to successfully execute several complex logical computations. iii) Multifunctionality as a vibration sensor is demonstrated by detecting vibrations along different axes induced by intentional mechanical deformation, highlighting its scalability for multiaxis strain input. Mechanical computing systems incorporating low-modulus and high-elongation materials enable flexible and stretchable innovative computing devices for technologies relying on the mechanical deformation of materials, such as wearable devices and soft robots. Furthermore, mechanical computing systems integrating active components hold significant potential for advancing automation and adaptive systems through complex signal processing.

Results

Logic-Device-Inspired Mechanical Computing System Based on 3D Cracked Optical Fiber

Mechanical computing device operation follows a conceptual flow where unit cells constituting the device interact through the input mechanical deformation and output a transformed state based on a deterministic nature (Fig. 1a). This study proposes a novel mechanical computing system in which the morphological state of optical fiber cracks is determined by input strain applied to the substrate[37–41], and light output with controlled attenuation is generated. Consequently, these cracked optical fibers function as diodes, actively modulating light transmission and distinguishing between on and off states, serving as active components within the mechanical computing system.

A diode is an active component in a semiconductor device that allows current to predominantly flow in one direction by controlling the carrier (hole or electron) concentration in the depletion region with an applied voltage bias, as shown in Fig. 1b. The on/off state of the diode is differentiated according to the threshold voltage, defined as the minimum forward bias required for the current to start flowing, beyond which the current begins to flow. Inspired by this operating mechanism, the cracked optical fiber switches the on/off state of light output by controlling the depletion level of light-carrying carriers (Fig. 1c). In contrast to designs using two separate fibers that connect and disconnect under strain, the crack-engineered single-fiber structure maintains precise core alignment, reduces misalignment under multi-axial deformation, and allows the switching threshold to be finely tuned through crack morphology control. Carrier depletion occurs in cracks intentionally created on the optical fiber surface and is regulated by the state of the three-dimensional (3D) crack, which varies with the applied strain. The strain-light-driven optical fiber diodes[42,43] can exhibit a rapid light attenuation behavior at the threshold strain, establishing a criterion to distinguish between the on and off states.

The strain-light-driven optical fiber diode operates through the deformation of cracked optical fibers attached to a low-modulus and high-elongation elastomeric substrate[44–49]. The mechanical properties of the elastomeric substrate enable it to endure reversible and repetitive deformation. Consequently, the architecture and operational mode of the cracked optical fibers are altered with the strain applied to the substrate, as shown in Fig. 1d. The crack of the optical fiber is formed in 3D[50–53] on the surface through a simple laser-cutting strategy, which is discussed in the succeeding section. The strain release exposes the optical fiber core region, which determines the light propagation path, leading to the attenuation of light transmission intensity[54–57]. The light transmission behavior of cracked optical fibers under varying strain applied to a pre-stretched elastomeric substrate is observed in bright field (Fig. 1e, left column) and dark field (Fig. 1e, right column). The transmitted light intensity attenuates owing to crack-induced light scattering and light carrier depletion as the applied strain to the substrate decreases (500, 250, and 0% strain). Moreover, nearly no light is transmitted into the fiber beyond the crack at conditions below approximately 180% strain (Fig. 1c). Consequently, the availability of cracked optical fibers as components of strain-light-driven mechanical computing devices is confirmed by inducing mechanical deformation and changing the state of individual cracked optical fibers independently or in combination by controlling the strain applied to the substrate (Fig. 1f). To determine the operational threshold for ON/OFF switching, a plot of transmitted light intensity versus applied strain was constructed. By applying linear extrapolation to the attenuation region, the intersection point with the intensity baseline was identified, corresponding to a threshold strain of approximately 180%. This point was used to define the effective strain-driven transition between the ON and OFF states of the device (see details in Supplementary Fig. 7).

Morphological Optimization of 3D Cracks for Effective Light Attenuation

Mechanical cracks are typically associated with structural weaknesses owing to stress concentration. Two-dimensional (2D) cracks weaken the strength and durability of materials and increase the risk of crack propagation, causing various challenges related to system stability. To address these problems, significant efforts have been made to effectively eliminate 2D cracks and maintain the structural integrity of materials. However, the potential of mechanical cracks as a strategic design element for systems requiring precise signal control, such as electronic sensors[58,59], has been explored. In particular, 3D cracks offer the advantage of precise control over stress distribution owing to their high spatial degree of freedom. This enables nonlinear responses to deformation and effective modulation of physical elements, such as light, vibration, and heat. In addition, 3D cracks enhance adaptability to complex mechanical stresses, ensuring stable performance under various deformation conditions. Consequently, systems using 3D cracks achieve superior sensitivity and precision under micro deformation, making them ideal for applications requiring finely tuned mechanical responses.

In this context, 3D cracks have been adopted as a structural strategy to achieve effective light attenuation and rapid on/off switching in optical fibers. Morphological optimization of cracks has been performed to maximize performance. The 3D cracks were formed by ablating a finite region of the fiber cladding using a straightforward and controllable laser-cutting method. Differences in the ablation of the fiber cladding area were induced by controlling the laser power; higher power intensities resulted in greater

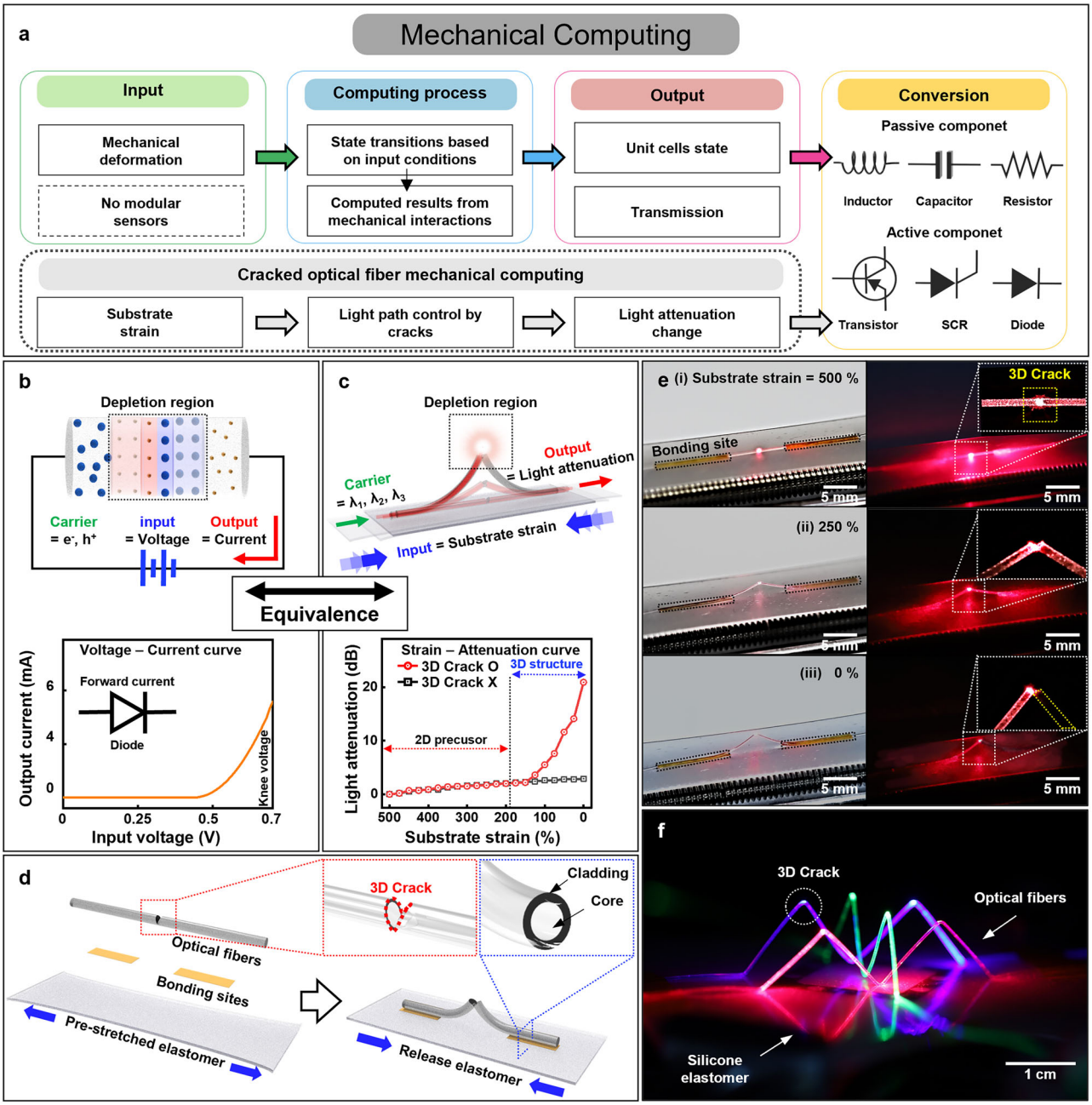

Fig. 1 | Schematics and Performance Analysis of Fiber-Optic-Based Mechanical Computing Systems. a Schematics illustrating the mechanical computing framework, from input to mechanical computing, output, and conversion. **b** Schematic of the depletion region formation in a typical diode, along with intensity and voltage graphs for forward bias. **c** Schematic of a fiber-optic-based mechanical computing unit and the strain and attenuation graphs resulting from the shrinkage of the silicone elastomer. **d** Schematic illustration of the fabrication method for a mechanical single unit and the components of the optical fiber. **e** Single unit cell images under substrain levels of (i) 500%, (ii) 250%, and (iii) 0%, with external light on (left), external light off (right), and zoomed-in view (inset). **f** Mechanical computing systems using unit cell arrays with different light wavelengths.

ablation, as shown in Fig. 2a–c. Although minor secondary cracks may form in the cladding region during the fabrication process, their influence on optical performance is expected to be minimal, as the device's ON/OFF functionality is primarily determined by the exposure of the fiber core through the engineered primary crack.

Subsequently, in-depth morphological analysis was performed to verify the 3D structural modification of the optical fiber after laser cutting. A 3D anisotropic crack was formed, exposing the core area—the primary light transmission path—under deformation (Fig. 2d, e).

To further understand the impact of 3D cracks, simulations were performed to obtain the stress distributions of the cracked optical fiber sensors. The simulations reveal the size and shape of the crack and the effect of that shape on the stress distribution. The stress distributions were evaluated for various crack shapes, including V-shape, two-point V-shape, and four-point V-shape (Fig. 2f–h). All stresses applied were below 4 MPa. Stress concentration is observed in the cracks, with the V-shaped cracks exhibiting more concentrated stress (Fig. 2f) compared with the more relaxed stress distributions observed in the two-point and four-point V-shaped cracks (Fig. 2g, h). Replicating experimental conditions, the optical fibers were fixed at both ends of the pre-stretched substrates elongated by up to 500%, followed by a controlled release to 300%. The stress distribution in each case was simulated around the cross-section of the 3D crack. These simulations

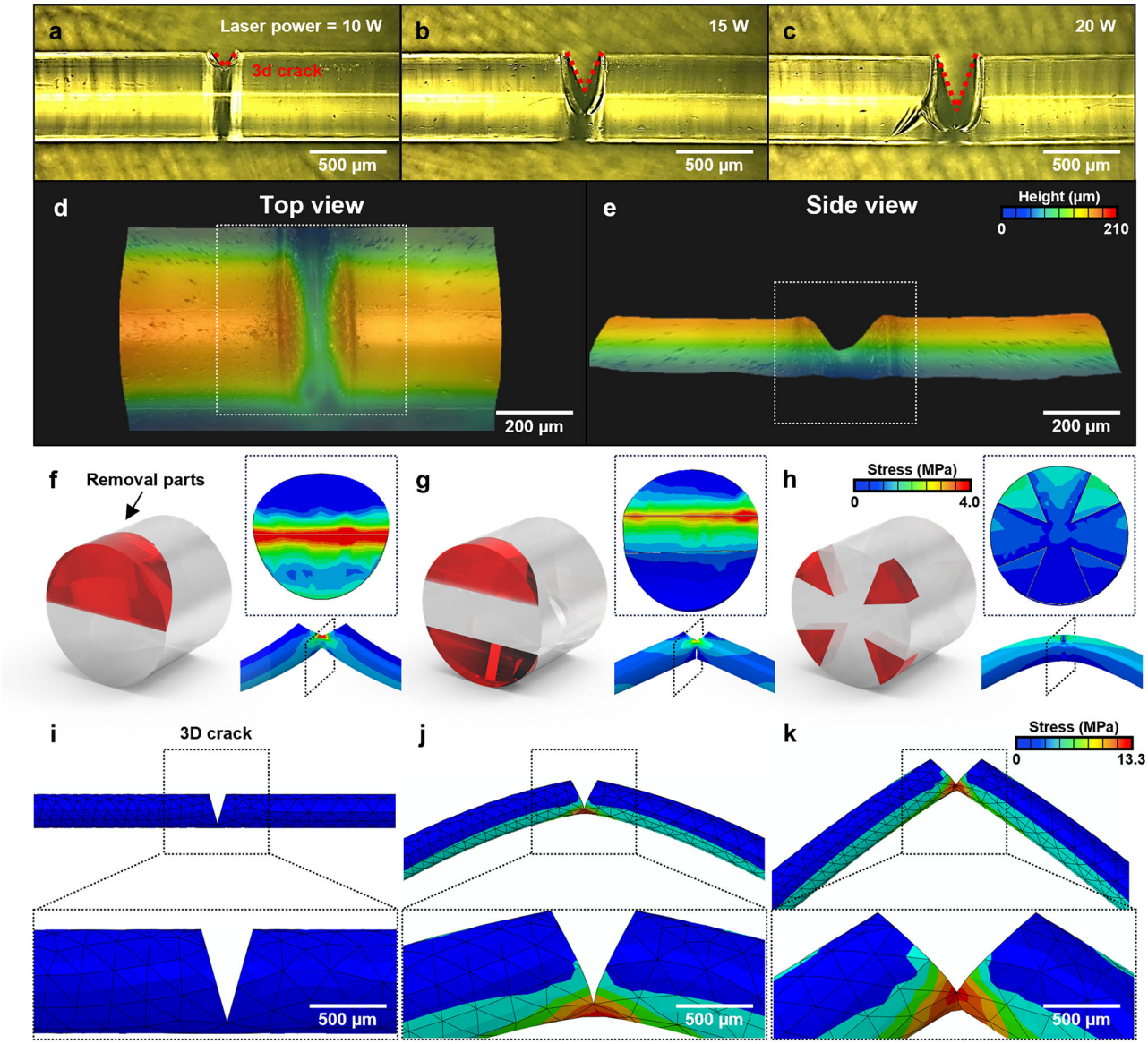

Fig. 2 | Crack Morphology and Stress Distribution in Laser-Cut Optical Fibers. OM images of crack sizes according to the power of the laser cutter: **a** 10 W, **b** 15 W, **c** 20 W. 3D profiler images of the cracked optical fiber: **d** top view, **e** side view. Stress distribution caused by different crack shapes: **f** V-shape, **g** Two-point V-shape, **h** Four-point V-shape. Stress distribution simulation of the V-shape unit under varying substrate strain: **i** 500%, **j** 250%, **k** 0%.

demonstrate how V-shaped cracks influence the stress distribution based on the substrate strain (Fig. 2i–k). In particular, stresses in the V-shaped cracks remain within safe limits, peaking at 13.3 MPa. To contextualize mechanical safety, the PMMA core exhibits a typical tensile strength of 60–70 MPa (bulk PMMA), yielding a factor-of-safety of ~4.5–5.3 at the maximum modeled stress (13.3 MPa). The applied strains and simulated stresses remained within the elastic regime throughout all experiments, and no plastic deformation or crack growth was observed under repeated cycling. This result aligns closely with experimental findings, highlighting the influence of anisotropic 3D crack geometry, generated through fiber cladding ablation, on stress concentration. During mechanical deformation of the optical fiber, stress tends to accumulate in uncut regions owing to this geometry. Upon substrate strain release, these concentrated stresses expose the fiber core, enhancing light attenuation and enabling efficient and swift transitions between the on/off states. Although mechanical stress anisotropy can potentially induce birefringence by shifting the refractive index, this effect is expected to be negligible in our system due to the highly localized nature of the stress induced at deliberately engineered crack regions. Furthermore, because our device's operation primarily relies on intensity modulation through crack-induced light leakage rather than phase or polarization modulation, the impact of birefringence on device performance is expected to be minimal.

Logic Computation Using an Active Signal Modulation Optical-Fiber-Based Mechanical Computing System

Leveraging the light attenuation and clear on/off state switching behavior of the cracked optical fiber diode, the logic computation performance of a mechanical computing system consisting of multiple cracked optical fibers was demonstrated (see details in the Experimental Section). This system defines the elongation state of the substrate as input and the intensity of light transmitted across the optical fiber crack as output (Fig. 3a). The input is defined as "0" when no change in elongation occurs, with the substrate remaining in a stretched state (Fig. 3a, upper column). Conversely, the input is defined as "1" when the elongation changes, corresponding to a released substrate (Fig. 3a, lower column). The output value is determined based on the total light intensity transmitted across the cracked optical fiber, which varies with the elongation state of the substrate. A threshold light intensity was set, adjustable depending on the system. Intensities below this threshold

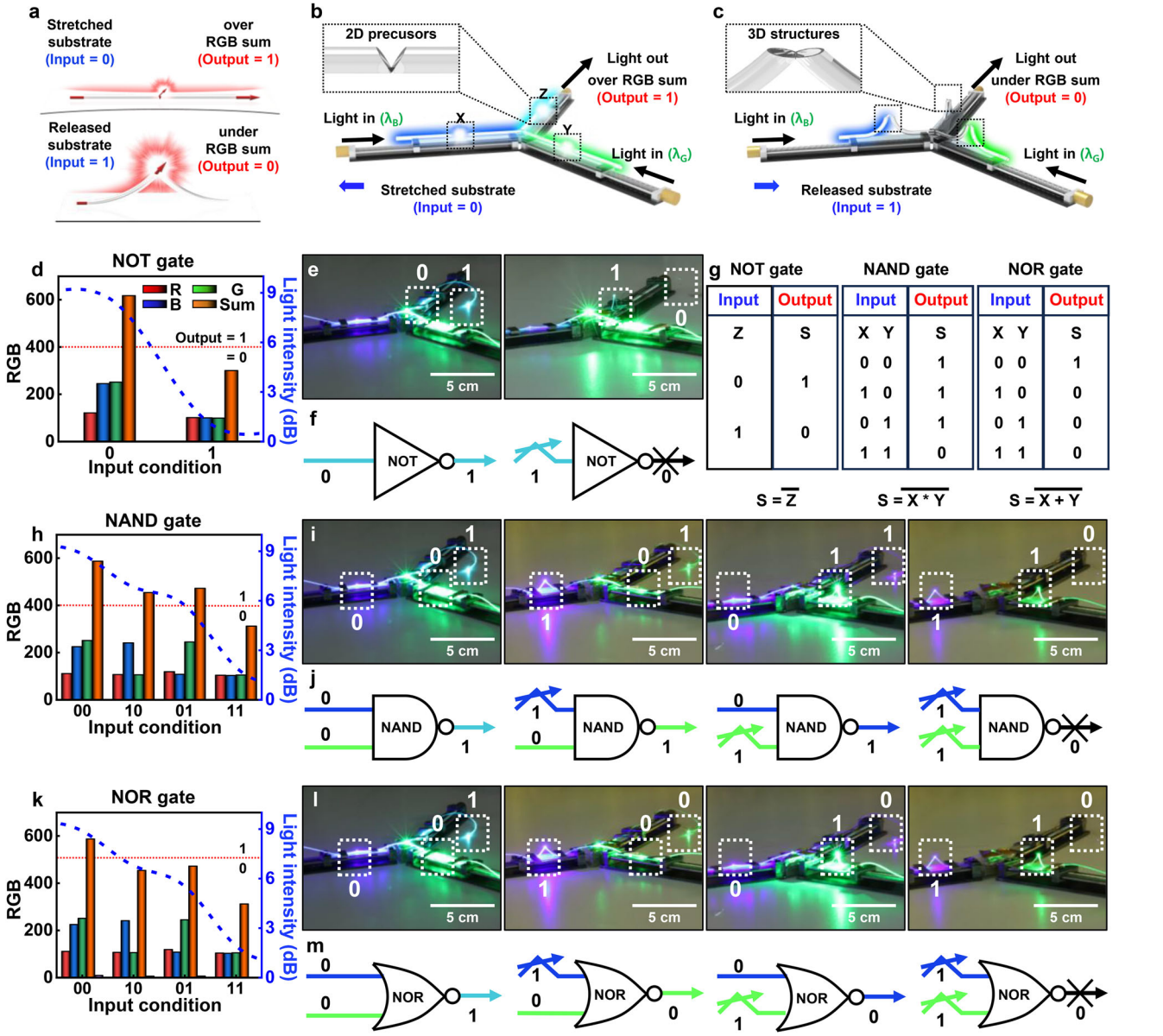

Fig. 3 | Optical Transistor Logic Gates in Mechanical Computing Systems. **a** Schematic of the input and output states of the mechanical computing unit cell. Three unit cells are used as switches for three transistors, acting as inputs X, Y, and Z. A laser beam is input into each part to measure the light emitted from other parts. **b** Schematic when input = 0 under substrate strain, where light is emitted outward. **c** Schematic when input = 1 under substrate strain, where light is not emitted outward. **d** RGB value graph detected at point "S" under the (01) and (10) logic conditions of a NOT gate. The output state is defined as "1" or "0" depending on whether the RGB sum exceeds 400. **e** Real image, **f** Schematic of the optical transistor NOT gate and its (01) and (10) logic conditions. **g** Truth table of logic gates defined by various input and output configurations. **h** RGB value graph detected at point "F" under the (001), (101), (011), and (110) logic conditions of a NAND gate. The output state is defined as "1" or "0" depending on whether the RGB sum exceeds 400. **i** Real image, **j** Schematic of the optical transistor NAND gate and its (001), (101), (011), and (110) logic conditions. **k** RGB value graph detected at point "F" under the (001), (100), (010), and (110) logic conditions of a NOR gate. The output state is defined as "1" or "0" depending on whether the RGB sum exceeds 500. **l** Real image, **m** Schematic of the optical transistor NOR gate and its (001), (101), (011), and (110) logic conditions.

were defined as an output value of "0" (Fig. 3a, lower column), whereas intensities exceeding the threshold were defined as an output value of "1" (Fig. 3a, upper column). Subsequently, three cracked optical fiber diodes were interconnected within the mechanical computing system to enable high-level computations. Different colored light sources are introduced into the cracked optical fiber diodes labeled "X" and "Y", while diode "Z" collects light transmitted through the two cracked optical fibers (Fig. 3b, c). For example, when no change in elongation is applied to all diodes (all input = "0"), the system outputs light exceeding the threshold intensity (output = "1") (Fig. 3b). Conversely, when elongation is removed from all diodes (all input = "1"), the output light intensity falls below the threshold (output = "0") (Fig. 3c).

The computational capabilities of various logic gates, comparable to those performed by electronic computers, were demonstrated using the mechanical deformation states of the substrate. A NOT gate was achieved by activating only diode Z (Fig. 3d). Regardless of the light intensity passing through fibers X and Y, when the "0" state (stretched state) was input to diode Z, the sum of the RGB light exceeded the threshold intensity, resulting in an output of "1". Conversely, with an input of "1" (released state) to diode Z, the RGB light sum remained below the threshold, yielding an output of "0". These results are visually discernible (Fig. 3e), successfully confirming the functionality of the NOT gate (Fig. 3f). In addition, NAND and NOR logic gates with complex input–output relationships were implemented by

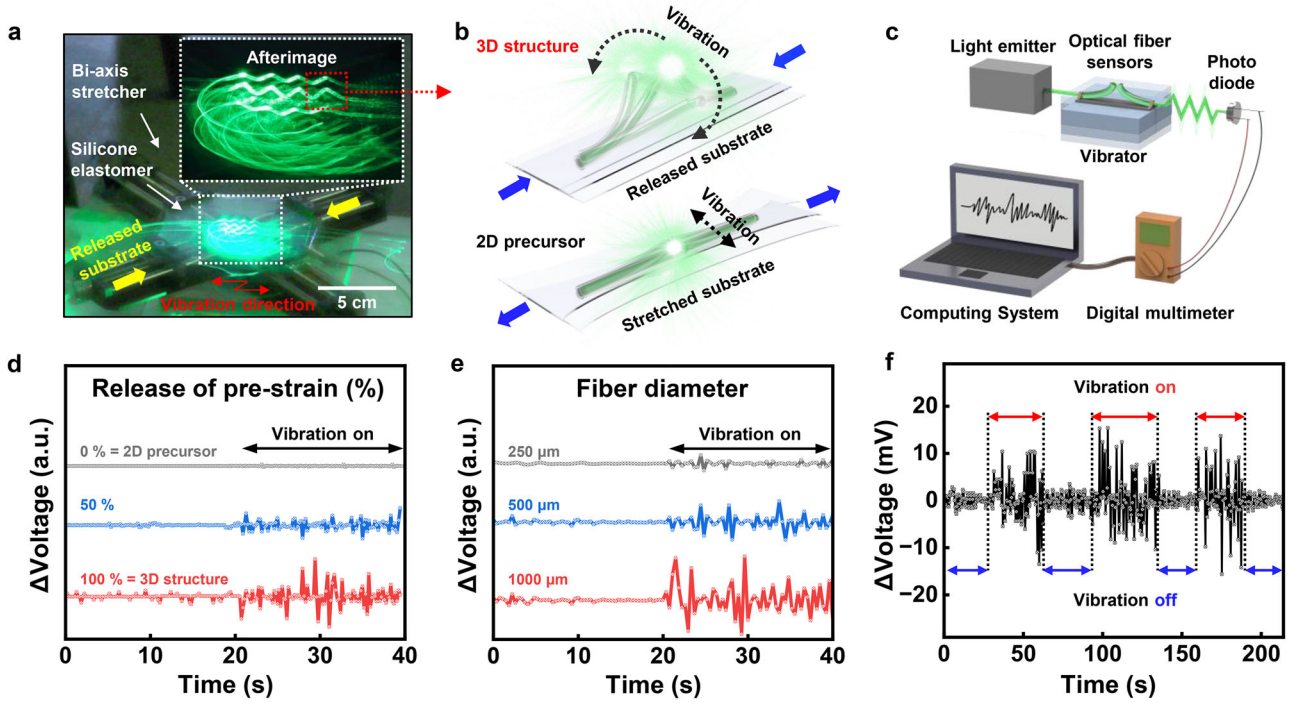

Fig. 4 | Vibration Sensing and Voltage Response in Cracked Optical Fiber Systems. a Photographs of the optical fiber under vibration. The mechanical computing array is designed with a pop-up structure using a bi-axis stretcher on a vibration motor. **b** Schematic of a single optical fiber unit cell vibrating. **c** Schematic of earthquake measurement using cracked optical fiber when Input = 1. **d** Voltage difference graph for three repeated cycles of vibration on/off. **e** Voltage measurement graph after adjusting the pop-up (0/50/100%) according to strain. **f** Voltage difference graph when vibration is on, based on the diameter of the optical fiber (250/500/1000 μm).

activating all cracked optical fibers in X and Y (Fig. 3g). Figure 3h–j and Fig. 3k–m illustrate the computing processes of the NAND and NOR gates, respectively. The computation results are consistent with the values in the logical operation table shown in Fig. 3g. Notably, the sum of light intensities reaching the end of diode Z, which determines the output value, was similar in the NAND and NOR logic circuit systems. However, both logic gates were successfully implemented by simply modifying the output threshold intensity setting.

Multifunctionality as a Multiaxis Vibration Sensor in a Mechanical Computing System

In a mechanical computing system, extending the input axis of deformation enables more complex and diverse calculations and improves computing performance by processing more information simultaneously. In this context, the scalability of the input axis for a strain-light-driven mechanical computing system was demonstrated by its ability to detect vibrations along an axis orthogonal to the prestrain applied to the substrate, as shown in Fig. 4a. Vibrations along this orthogonal axis distort the light transmission path, reducing the intensity of the transmitted light. Notably, the attenuation of light transmission owing to vibration becomes more pronounced when the core of the cracked optical fiber is exposed as the prestrain is released (Fig. 4b). Accordingly, the light transmitted through the cracked optical fiber under a vibrational environment and the voltage change was observed (Fig. 4c). Depending on the degree of prestrain release, i.e., the degree to which the 3D crack of the optical fiber is exposed, different voltage changes are observed (Fig. 4d). When the prestrain remains unreleased, the crack exposure area is extremely small, and light scattering is negligible, even when the light transmission path is distorted owing to vibration. By contrast, with an enlarged crack exposure area owing to increased strain release, a significant voltage change is observed. In addition, increasing the diameter of the cracked optical fiber maximizes light scattering under the same vibration condition, resulting in higher sensitivity to changes in the intensity of the transmitted light (Fig. 4e). Furthermore, the system demonstrated sufficient temporal resolution to distinguish continuous vibrations alternating between the on/off states at specific time intervals (Fig. 4f). These findings highlight the capability of the system to sense multiaxis mechanical strain inputs. This implies that strain-light-driven mechanical computing systems have the potential to sense diverse physical changes and perform multifunctional computations on complex inputs.

The vibration sensing experiment in Fig. 4f was conducted with a time resolution of ~0.375 s per data point (80 points per 30 s cycle). The system exhibited an optical-electrical response time of approximately 2.3–2.8 s to changes in vibration state. The 30-second interval between cycles was set to minimize residual deformation effects. While this configuration prioritized multifunctionality demonstration over fast dynamic sensing, future optimization of crack geometry and material response is expected to improve temporal performance (see details in Supplementary Fig. 8).

Discussion

This study proposed a logic-device-inspired mechanical computing system capable of signal modulation, a typical function of active components, by integrating soft and 3D electronics. The proposed system was designed by integrating 3D cracked optical fibers with a low-modulus, high-elongation elastomeric substrate to enable a multimodal architecture of the 3D cracked optical fibers that responds the reversible deformation of the substrate. The optimized crack morphology was engraved onto the optical fiber using a laser-cutting strategy supported by simulation studies. These engraved cracks induced stress concentration in specific regions when the optical fiber deformed under strain. Stress concentration induced light carrier depletion and rapid attenuation of light output, demonstrating that the cracked optical fiber functioned as a diode, exhibiting on/off state switching behavior. Furthermore, logical calculations were successfully performed by integrating multiple cracked optical fiber diodes into a mechanical computing system. The system demonstrated multifunctional vibration sensing, capable of detecting vibrations with orthogonal axes to the prestrain, highlighting its axis scalability for strain input. Furthermore, this study explored

three-dimensional structures, such as helical configurations, demonstrating that the stress concentration and optical attenuation mechanisms induced by cracks can also be applied to optical fibers with non-linear morphologies. This enables their use as mechanical computing elements capable of responding to various types of deformations (Supplementary Information Figs. 1–6). The anisotropic nature of the helical structures enable stress concentration under external deformation, induces light attenuation, and offer excellent durability under high strain and stress. Given the mechanical stability of optical fiber below its glass transition temperature and its tolerance to moderate radiation doses (see Materials in Method section), the system is expected to maintain stable operation under harsh environmental conditions, and its potential has been demonstrated through integration with application scenarios involving physical deformation. In this regard, strain-light-driven mechanical computing systems based on optical fibers with structural degrees of freedom are expected to revolutionize applications in various fields, such as robotics and space exploration (see details in Supplementary Fig. 9 and Supplementary Table 1).

Methods

Materials

The optical fiber employed in this study was the Toray PG series fibers, each comprising a polymethyl methacrylate (PMMA) core and a fluorinated-polymer cladding. Key specifications are: an operating temperature range of −55 °C to +70 °C; attenuation ≤0.20 dB/m at 650 nm; the glass transition temperature (~ 100 °C); and radiation tolerance of several hundred grays to a few kilo grays.

Fabrication of Silicone Elastomer

PMMA (≈ 100 nm, Microchem INC) was spin-coated on a silicon wafer (3000 rpm for 30 s). After spin-coating, a three-step soft-bake process was conducted. The wafer was sequentially heated on a hotplate at 110, 160, and 180 °C, each for 10 min. Subsequently, the silicone elastomer (Ecoflex 0050, Smooth-on) was prepared by mixing the base (Part A) and curing agent (Part B) in a 1:1 ratio. After mixing, 20 g of the silicone elastomer was spin-coated on a the PMMA-coated wafer, followed by spin-coating at 1000 rpm for 1 s, repeated three times. Semi-curing was performed at 110 °C on a hotplate for 1 min, followed by full curing at 25 °C for 24 h.

Fabrication and Characterization of Cracked Optical Fiber

A laser cutter (JQ laser, JQ9060) was used to create cracks in the optical fiber (Toray, PGR-FB). The power and speed settings of the laser were adjusted to control the dwell time and intensity of the laser beam to form 3D cracks. The laser cutter was operated at a speed of 10 mm/s, with optimized power settings to ensure uniform and controlled 3D crack formation. The parameters of the laser cutter, including speed (mm/s) and power (W), were optimized to ensure controlled crack formation. The crack patterns were designed considering the interaction between the laser and optical fiber material to achieve precise 3D cracks.

Fabrication of Bonding Sites and Integrated Devices

Multiple bonding techniques were employed to integrate the elastomeric substrate with the 3D cracked optical fiber. Siloxane bonding was used for optical fibers with diameters ranging from 250 to 500 μm. Using photolithography and an e-beam evaporator, 100 nm SiO_2 and 100 nm Ti layers were selectively deposited onto the 3D cracked optical fibers through a masking process. The elastomeric substrate was heated to 60 °C and placed in conformal contact with the optical fibers. A paper towel was placed over the substrate, and a 1 kg weight was applied for 30 min to ensure proper bonding. Polyimide tape was laser cut for fibers exceeding 500 μm in diameter to match the bonding area, facilitating easy integration with stronger adhesion. Siloxane bonding enabled microscale precision, while polyimide tape bonding provided robust adhesion suitable for various fiber sizes.

Fabrication and Measurement of Vibration Sensors

Vibration sensor experiments were conducted in a dark room to eliminate external light interference. One end of the cracked optical fibers was connected to a light emitter, directing light through the fiber. The other end of the fiber was connected to a photodiode linked to a digital multimeter (2400 SMU, Keithley). The substrate, with the cracked optical fibers attached, was placed on a high-speed motor-equipped stage. As the motor vibrated the substrate, the vibration modulated the light output of the fiber, and the current of the photodiode was measured to quantify the sensor response.

Fabrication and Measurement of Logic Gates

Three cracked optical fiber diodes were connected using a Y-shaped connector to create logic gate structures. Light sources with three distinct wavelengths (λR = 655 nm, λG = 532 nm, and λB = 460 nm) were used as inputs. The strain applied to the prestrained substrate, adjusted using the X and Y stretchers of the diodes, served as the input signal. Although the color of the output light could be visually observed, quantitative analysis was performed by capturing images and measuring RGB pixel intensities in a defined area using the ImageJ software.

Fabrication and Measurement of Helical Optical Fiber Sensors

Optical fibers (Toray, FBG-PGR) were coiled around a rod and fixed using polyimide tape. The fibers were then heat-annealed in a vacuum oven at 70 °C for 1 h, followed by cooling to room temperature for 10 min. After cooling, the tape was removed, and the fibers were carefully unwound to form helical optical fiber sensors. One end of the fiber was illuminated with a laser pointer to measure strain, while the other was connected to an optical power meter. For pressure measurements, the sensor was encapsulated in PDMS to ensure even pressure distribution (0–50 N) applied using a universal testing machine (UTM).

Finite Element Analysis (FEA)

Finite element analysis (FEA) simulations were performed using Abaqus to evaluate the mechanical response of the cracked optical fiber sensors. The optical fiber was modeled as a cylindrical structure with a diameter of 0.25 mm, featuring a crack measuring 0.13 mm in width and 0.23 mm in length. Due to the geometric complexity around the crack region, 10-node quadratic tetrahedron elements (C3D10) were employed[60]. A global seed size of 0.1 was applied, resulting in 12,402 elements. This mesh density provides higher accuracy compared to those used in previous convergence studies[61,62]. The material properties of the optical fiber were defined based on experimental stress–strain (S-S) data, with a Young's modulus of 1121 MPa and Poisson's ratio of 0.16. The optical fiber was pre-stretched by 500% and then released to 300%, simulating the experimental conditions. The simulation results were consistent with the experimental data, demonstrating that strain concentration occurred in areas with lower modulus around the cracks, confirming the accuracy of the model.

Data availability

The data that support the findings of this study are either provided in the source data or are available from the corresponding author upon reasonable request.

Received: 11 March 2025; Accepted: 23 October 2025;
Published online: 28 November 2025

References

1. Yasuda, H. et al. Mechanical computing. *Nature* **598**, 39–48 (2021).
2. Lee, T.-H., Bhunia, S. & Mehregany, M. Electromechanical computing at 500°C with silicon carbide. *Science* **329**, 1316–1318 (2010).
3. Merkle, R. C. et al. Mechanical computing systems using only links and rotary joints. *J. Mech. Robot.* **10**, 061006 (2018).
4. Merkle, R. C. Two types of mechanical reversible logic. *Nanotechnol* **4**, 114–131 (1993).

5. Chowdhury, F. K., Choe, D., Jevremovic, T. & Tabib-Azar, M. Design of MEMS based XOR and AND gates for rad-hard and very low power LSI mechanical processors. *Proc*. IEEE Sensors 762–765 (2011).
6. Li, Y. et al. Reprogrammable and reconfigurable mechanical computing metastructures with stable and high-density memory. *Sci. Adv* **10**, eado6476 (2024).
7. El Helou, C. et al. Mechanical metamaterials for computing and robotics. *Nature* **608**, 699–704 (2022).
8. Byun, J., Pal, A., Ko, J. & Sitti, M. Integrated mechanical computing for autonomous soft machines. *Nat. Commun.* **15**, 2933 (2024).
9. Mei, T. & Chen, C. Q. In-memory mechanical computing. *Nat. Commun.* **14**, 5204 (2023).
10. Raney, J. R. et al. Stable propagation of mechanical signals in soft media using stored elastic energy. *Proc. Natl. Acad. Sci. USA* **113**, 9722–9727 (2016).
11. Treml, B. et al. Origami mechanologic. *Proc. Natl. Acad. Sci. USA* **115**, 6916–6921 (2018).
12. Vo, V. T. et al. Sheet-based fluidic diodes for embedded fluidic circuitry in soft devices. *Adv. Intell. Syst.* **6**, 2300785 (2024).
13. Coulais, C. et al. Combinatorial design of textured mechanical metamaterials. *Nature* **535**, 529–532 (2016).
14. Song, Y. et al. Additively manufacturable micro-mechanical logic gates. *Nat. Commun.* **10**, 882 (2019).
15. Chen, T., Mueller, J. & Shea, K. Intergrated design and simulation of tunable, multi-state structures fabricated monolithically with multi-material 3D printing. *Sci. Rep.* **7**, 45671 (2017).
16. Bilal, O. R. et al. Intrinsically polar elastic metamaterials. *Adv. Mater.* **29**, 1700540 (2017).
17. Shan, S. et al. Multistable architected materials for trapping elastic strain energy. *Adv. Mater.* **27**, 4296–4301 (2015).
18. Jiang, Y., Korpas, L. M. & Raney, J. R. Bifurcation-based embodied logic and autonomous actuation. *Nat. Commun.* **10**, 128 (2019).
19. Jin, L. et al. Guided transition waves in multistable mechanical metamaterials. *Proc. Natl Acad. Sci. Usa.* **117**, 2319–2325 (2020).
20. Horsman, C. et al. When does a physical system compute? *Proc. Math. Phys. Eng. Sci.* **470**, 20140182 (2014).
21. Feynman, R. Feynman Lectures on Gravitation. (CRC Press, 2018).
22. Tucker, R. S. The role of optics in computing. *Nat. Photon.* **4**, 405–406 (2010).
23. Liang, Y. et al. A review of rechargeable batteries for portable electronic devices. *InfoMat.* **1**, 6–32 (2019).
24. Wang, Y. et al. Binary-phase acoustic passive logic gates. *Sci. Rep.* **9**, 8355 (2019).
25. Kim, J. H. et al. Next-generation sensors with three-dimensional micro-/nano-structures. *J. Sens. Sci. Technol.* **33**, 419–425 (2024).
26. Fyrigos, I.-A. et al. Wave computing with passive memristive networks **12**, 16 (2023).
27. Saengchairat, N., Tran, T. & Chua, C.-K. A review: Additive manufacturing for active electronic components. *Virtual Phys. Prototyp.* **12**, 31–46 (2017).
28. Ostmann, A. et al. Intergration of passive an active componets into build-up layers. In 4th Electronics Packaging Technology Conference, (EPT, 2002).
29. Allendorf, M. D. et al. A roadmap to implementing metal–organic frameworks in electronic devices: challenges and critical directions. *Chemistry* **17**, 11372–11388 (2011).
30. Shan, Z. et al. Phonon-assisted electro-optical switches and logic gaes based on semiconductor nanostructures. *Adv. Mater.* **31**, 1901263 (2019).
31. Zadegan, R. M. et al. Construction of a fuzzy and boolean logic gates based on DNA. *Small* **11**, 1811–1817 (2015).
32. El Helou, C. et al. Digital logic gates in soft, conductive mechanical metamaterials. *Nat. Commun.* **12**, 1633 (2021).
33. Mei, T. et al. A mechanical metamaterial with reprogrammable logical functions. *Nat. Commun.* **12**, 7234 (2021).
34. Meng, Z. et al. Bistability-based foldable origami mechanical logic gates. *Extrem. Mech. Lett.* **43**, 101180 (2021).
35. Pashkevich, A., Klimchik, A. & Chablat, D. Enhanced stiffness modeling of manipulators with passive joints. *Mech. Mach. Theor.* **46**, 662–679 (2011).
36. Li, H. et al. Reverse engineering of the giant muscle protein titin. *Nature* **418**, 998–1002 (2002).
37. Lee, S. E. et al. Active-type piezoelectric smart textiles with antifouling performance for pathogenic control. *NPJ Flex. Electron* **8**, 65 (2024).
38. Jung, Y. H. et al. A wireless haptic interface for programmable patterns of touch across large areas of the skin. *Nat. Electron.* **5**, 374–381 (2022).
39. Kim, J. J. et al. Skin electronics: next-generation device platform for virtual and augmented reality. *Adv. Funct. Mater.* **31**, 2009602 (2021).
40. Dai, Y. et al. Wearable sensor patch with hydrogel microneedles for in situ analysis of interstitial fluid. *ACS Appl. Mater. Interfaces* **15**, 56760–56767 (2023).
41. Kim, B. H. et al. Three-deimensional electronic microfliers inspired by wind-dispersed seeds. *Nature* **597**, 503–510 (2021).
42. Fan, L. et al. An all-silicon passive optical diode. *Science* **335**, 447–450 (2012).
43. Ai, L. et al. Concentration-switchable assembly of carbon dots for circularly polarized luminescent amplificatin in chiral logic gates and deep-red light-emitting diodes. *Adv. Mater.* **36**, 2410094 (2024).
44. Kim, J. H. et al. Applications of flexible and stretchable three-dimensional structures for soft electronics. *Soft Sci*. **3**, https://doi.org/10.20517/ss.2023.07 (2023).
45. Lee, S. E. et al. Reversible solar heating and radiative cooling devices via mechanically guided assembly of 3D macro/microstructures. *Adv. Mater.* **36**, 2400930 (2024).
46. Zhao, H. et al. Mechanially guided hierarchical assembly of 3D mesostructures. *Adv. Mater.* **34**, 2109416 (2022).
47. Ryu, H. et al. Transparens, compliant 3D mesostructures for precise evaluation of mechanical characteristics of organoids. *Adv. Mater.* **33**, 2100026 (2021).
48. Xue, Z. et al. Mechanically-guided structural designs in stretchable inorganic electronics. *Adv. Mater.* **32**, 1902254 (2020).
49. Huang, X. et al. Intelligent soft sweat sensors for the simultaneous healthcare monitoring and safety warning. *Adv. Healthc. Mater.* **12**, 2202846 (2023).
50. Park, J. H. et al. 2D MoS_2 helical liquid crystalline fibers for multifunctional wearable sensors. *Adv. Fiber Mater.* **1**, 1–10 (2024).
51. Elsherif, M. et al. Optical fiber sensors: working principle, applications, and limitations. *Adv. Photon. Res.* **3**, 2100371 (2022).
52. Zhang, S. et al. Fibers/textiles-based flexible sweat sensors: a review. *ACS Mater. Lett.* **5**, 1420–1430 (2023).
53. Meng, L. et al. High-accuracy 3D shape sensor based on anti-twist packaged high uniform multicore fiber FBGs. *Adv. Fiber Mater.* **5**, 1467–1480 (2023).
54. Xiao, A. et al. A degradable bioelectronic scaffold for localized cell transfection toward enhancing wound healing in a 3D space. *Adv. Mater.* **36**, 2404534 (2024).
55. Shin, J. H. et al. Induced robust cu electrode on glass substrates and its applicaion for thin-film μLEDs. *Adv. Mater.* **33**, 2007186 (2021).
56. Park, Y. G. et al. High-resolution 3D printing for elctronics. *Adv. Sci.* **9**, 2104623 (2022).
57. Li, X. et al. Micromechanisms of macrocrack propagation behavior affected by short to long fatigue microcracks. *Mech. Adv. Mater. Struct.* **29**, 2726–2740 (2022).
58. Im, D. et al. Effect of adhesion strength between flexible substrates and electrodes on the durability of electrodes. *J. Sens. Sci. Technol.* **33**, 86–94 (2024).
59. Jeong, D. H. et al. Fabrication and evaluation of single layer graphene/SnO_2 based gas sensor for NO_2 detection. *J. Sens. Sci. Technol.* **33**, 493–501 (2024).

60. Sadighi, M. & Hosseini, S. A. Finite element simulation and experimental study on mechanical behavior of 3D woven glass fiber composite sandwich panels. *Compos. Part B Eng* **55**, 158–166 (2013).
61. Yang, W. et al. Tensile-after-ablation progressive damage and the failure mechanism of 2.5D woven composites with crack pores. *Polym. Compos.* **45**, 4014–4030 (2024).
62. Panwar, A. A. & Neelakrishnan, S. An exploration on the numerical investigation of 3D laminated composites with carbon fibre tow modelling using SwiftComp module in ABAQUS. *Mater. Today Proc*. https://doi.org/10.1016/j.matpr.2023.05.726 (2023).

Acknowledgements

This work was supported by the National Research Foundation of Korea (NRF) grant funded by the Korea government (MSIT) (grant Nos. RS-2024-00347619, RS-2024-00406240, RS-2024-00407155, RS-2025-00513522, and RS-2025-25420118). This research was supported by a grant of Korean ARPA-H Project through the Korea Health Industry Development Institute (KHIDI), funded by the Ministry of Health & Welfare, Republic of Korea (grant number: RS-2025-25454431).

Author contributions

J.H.P., J.H.K., and H.U.C. contributed equally to this work. J.H.P., J.H.K., and H.U.C. conducted most of the experiments. B.H.K. conceived the idea and supervised the overall work. J.K., H.L., J.K., and B.H.K. conceived of the overall research goals and aims. J.S.C., H.K., S.E.L., S.K., and H.J.J. supported the experiments. All authors discussed the results and commented on the manuscript.

Competing interests

The authors declare no competing interests.

Additional information

Supplementary information The online version contains supplementary material available at https://doi.org/10.1038/s41528-025-00497-2.

Correspondence and requests for materials should be addressed to Jiwoong Kim, Heon Lee, Jaehwan Kim or Bong Hoon Kim.

Reprints and permissions information is available at http://www.nature.com/reprints

Publisher's note Springer Nature remains neutral with regard to jurisdictional claims in published maps and institutional affiliations.

Open Access This article is licensed under a Creative Commons Attribution-NonCommercial-NoDerivatives 4.0 International License, which permits any non-commercial use, sharing, distribution and reproduction in any medium or format, as long as you give appropriate credit to the original author(s) and the source, provide a link to the Creative Commons licence, and indicate if you modified the licensed material. You do not have permission under this licence to share adapted material derived from this article or parts of it. The images or other third party material in this article are included in the article's Creative Commons licence, unless indicated otherwise in a credit line to the material. If material is not included in the article's Creative Commons licence and your intended use is not permitted by statutory regulation or exceeds the permitted use, you will need to obtain permission directly from the copyright holder. To view a copy of this licence, visit http://creativecommons.org/licenses/by-nc-nd/4.0/.

© The Author(s) 2025